Table 2 Oligosaccharide linkages for culture and surface seawater UDOM

	Culture			Oosterschelde			Hawaii			Woods Hole		
	T*	B	NB	T	B	NB	T	B	NB	T	B	NB
Arabinose (f)†	100	0	0	100	0	0	100	0	0	100	0	0
Arabinose (p)‡	25	33 (1, 3, 4)	42 (1, 3)	31	0	68 (1, 3)	18	48 (1, 3, 4)	34 (1, 3)	55	0	45 (1, 3)
Rhamnose	22	4 (1, 3, 4)	43 (1, 3) 27 (1, 4)	54	9 (1, 3, 4)	22 (1, 3) 17 (1, 4)	60	27 (1, 3, 4)	10 (1, 3) 3 (1, 4)	78	0	11 (1, 3) 11 (1, 4)
Fucose	36	24 (1, 3, 4)	12 (1, 3) 26 (1, 4)	34	29 (1, 3, 4)	37 (1, 3)	47	4 (1, 3, 4)	43 (1, 3) 6 (1, 4)	72	9 (1, 3, 4)	19 (1, 3)
Xylose	50	24 (1, 3, 4)	3 (1, 3) 12 (1, 4) 10 (2, 3)	24	54 (1, 3, 4)	2 (1, 3) 6 (1, 4) 13 (2, 3)	28	30 (1, 3, 4)	9 (1, 3) 33 (1, 4)	79	10 (1, 3, 4)	4 (1, 3) 6 (1, 4)
Mannose	11	30 (1, 3, 4)	31 (1, 2) 6 (1, 4) 14 (1, 6) 9 (3, 6)	9	29 (1, 3, 4)	25 (1, 2) 6 (1, 4) 3 (1, 6) 25 (3, 6)	20	15 (1, 3, 4)	21 (1, 2)	19	25 (1, 3, 4)	16 (1, 2)
Galactose	33	29 (1, 3, 4)	10 (1, 3) 28 (1, 6)	9	24 (1, 3, 4) 55 (3, 4, 6)	6 (1, 3) 5 (1, 6)	25	36 (1, 3, 4)	29 (1, 3)	55	33 (1, 3, 4)	12 (1, 3)
Glucose	21	64 (1, 3, 4)	15 (1, 3)	18	56 (1, 3, 4)	25 (1, 3)	7	0	80 (1, 3) 14 (1, 2)	39	28 (1, 3, 4)	32 (1, 3)

Each entry shows the percentage per sugar of a particular linkage type, followed (for branched and non-branched types) by numbers in parentheses describing the linkages.
* T, terminal; B, branched; NB, non-branched.
† Furanose form.
‡ Pyranose form.

Previous studies of DOC composition and cycling have emphasized the role of geopolymerization reactions in the production of structurally complex, metabolically resistant organic matter. The recent report of bacterial porin-like proteins dissolved in sea water demonstrates the potential for a contribution from resistant biopolymers[18]. Our study extends this concept to a quantitatively significant fraction of DOC, where a family of closely related acyl-oligosaccharides formed by direct biosynthesis contributes up to 70% of UDOM and 20% of total DOC in surface sea water. The very similar monosaccharide composition of surface and deep-sea UDOM suggests that some fraction of these oligosaccharides may survive over long timescales and contribute a significant fraction of the total marine DOC[12,18]. Further work detailing the chemical structure, potential sources, and metabolism of these oligosaccharides is needed to understand better the link between algal production of DOC, and its accumulation in surface sea water. □

Received 23 July 1996; accepted 26 March 1997.

1. Hedges, J. I. Global biogeochemical cycles: progress and problems. *Mar. Chem.* **39,** 67–93 (1992).
2. Peltzer, E. & Hayward, N. A. Spatial and temporal variability of total organic carbon along 140° W in the equatorial Pacific Ocean in 1992. *Deep-Sea Res. II* **43,** 1155–1180 (1996).
3. Chopin-Montegut, G. & Avril, B. Vertical distribution and temporal variation of dissolved organic carbon in the North-Western Mediterranean Sea. *Deep-Sea Res.* **40,** 1963–1972 (1993).
4. Williams, P. M. & Gordon, L. I. Carbon-13: carbon-12 ratios in dissolved and particulate organic matter in the sea. *Deep-Sea Res.* **17,** 19–27 (1970).
5. Druffel, E. R. M., Williams, P. M., Bauer, J. E. & Ertel, J. R. Cycling of dissolved and particulate organic matter in the open ocean. *J. Geophys. Res.* **97,** 15639–15659 (1992).
6. Menzel, D. in *The Sea* Vol. 5 (ed. Goldberg, E. D.) 659–678 (Wiley-Interscience, New York, 1974).
7. Carlson, C. A., Ducklow, H. W. & Michaels, A. F. Annual flux of dissolved organic carbon from the euphotic zone in the northwestern Sargasso Sea. *Nature* **371,** 405–408 (1994).
8. Benner, R., Pakulski, J. D., McCarthy, M., Hedges, J. I. & Hatcher, P. G. Bulk chemical characterization of dissolved organic matter in the ocean. *Science* **255,** 1561–1564 (1992).
9. Santschi, P. H. *et al.* Isotopic evidence for the contemporary origin of high molecular weight organic matter in oceanic environments. *Geochim. Cosmochim. Acta* **59,** 625–631 (1995).
10. Buesseler, K. O. *et al.* An intercomparison of cross-flow filtration techniques used for sampling marine colloids. Overview and organic carbon results. *Mar. Chem.* **55,** 1–32 (1996).
11. Sakugawa, H. & Handa, N. Isolation and chemical characterization of dissolved and particulate polysaccharides in Mikawa Bay. *Geochim. Cosmochim. Acta* **49,** 1185–1193 (1985).
12. McCarthy, M. D., Hedges, J. I. & Benner, R. The chemical composition of dissolved organic matter in seawater. *Chem. Geol.* **107,** 503–507 (1993).
13. Pazur, J. H. in *Carbohydrate Analysis* (eds Chaplin, M. F. & Kennedy, J. F.) 55–96 (IRL, Washington, 1986).
14. Painter, T. J. in *The Polysaccharides* Vol. 2, Ch. 4 (ed. Aspinol, G. O.) 196–285 (Academic, New York, 1983).
15. Gagosian, R. B. & Stuermer, D. H. The cycling of biogenic compounds and their diagenetically transformed products in seawater. *Mar. Chem.* **5,** 605–632 (1977).
16. Harvey, G. R., Boran, D. A., Chesal, L. A. & Tokar, J. M. The structure of marine fulvic and humic acids. *Mar. Chem.* **12,** 119–132 (1983).
17. Mopper, K. *et al.* The role of surface-active carbohydrates in the flocculation of a diatom bloom in a mesocosm. *Deep-Sea Res. II* **42,** 47–73 (1995).
18. Tanoue, E., Nishiyama, S., Kamo, M. & Tsugita, A. Bacterial membranes: Possible source of a major dissolved protein in seawater. *Geochim. Cosmochim. Acta* **59,** 2643–2648 (1995).
19. Vernon-Clark, R. N., Goldberg, E. D. & Bertine, K. K. Organic and inorganic characterization of marine colloids. *Chem. Ecol.* **11,** 69–83 (1996).

Acknowledgements. We thank V. Klap (Netherlands Institute of Ecology) for supplying the Oosterschelde seawater sample, and C. Johnson for assistance with acquiring GC/MS and NMR spectra. This work was supported by the US Department of Energy Ocean Margins Program.

Correspondence and requests for materials should be addressed to D.J.R.

Changes of the Earth's rotation axis owing to advection of mantle density heterogeneities

Bernhard Steinberger* & Richard J. O'Connell

Department of Earth and Planetary Sciences, Harvard University, Cambridge, Massachusetts 02138, USA

Polar wander, the secular motion of the Earth's rotation axis relative to its surface, has been studied for many years. Dynamical arguments[1–3] show that polar wander can arise from the redistribution of mass in a plastic deformable Earth, the rate depending on both the rate of mass redistribution and the rate at which the Earth's rotational bulge can readjust to the changing rotation axis. Here we use a viscosity structure obtained through geoid modelling[4], a mantle flow field consistent with tomographic anomalies[5], and time-dependent lithospheric plate motions[6] to calculate the advection of mantle density heterogeneities and corresponding changes in the degree-two geoid during the Cenozoic era. We show that the rotation axis will follow closely any imposed changes of the axis of maximum non-hydrostatic moment of inertia. The resulting path of the rotation axis agrees well with palaeomagnetic results[7], with the model predicting a current rate of polar motion that explains 40% of that observed geodetically[8].

* Present address: Institute of Meteorology and Geophysics, University Frankfurt, 60323 Frankfurt, Germany

The rotational bulge tends to stabilize the location of the pole, but the bulge can readjust by plastic flow to a change in the position of the rotation axis. If the timescale for the adjustment of the bulge is short enough, the location of the rotation pole is determined by the location of the greatest principal moment of inertia based on the non-hydrostatic density distribution (that is, with the contribution of the hydrostatic bulge removed). The non-hydrostatic moments of inertia, however, depend on the density distribution in the Earth's mantle, which may change with time owing to thermal convection and tectonic plate motion. The density distribution in the Earth has been inferred from seismic velocity variations and has been related to the non-hydrostatic geoid with dynamical models[9,10]. In these models the density anomalies cause flow in the viscous mantle, and a consequence is that the density anomalies are carried by the flow, and their distribution is time-dependent.

The path of the axis of maximum non-hydrostatic moment of inertia in Fig. 1 was calculated using the following steps. (1) The present-day distribution of shear velocity heterogeneity in the mantle is obtained from seismic tomography[5]. (2) Seismic velocity anomalies are converted to density anomalies[4,11]. (3) Time-dependent plate velocities and geometries[6] are used to model plate motions during the past 64 million years. (4) A previously proposed viscosity structure[4] (Fig. 1) is adopted for the mantle. (5) A mantle flow field that satisfies the boundary conditions on surface plate velocity and is driven by the internal density heterogeneities is calculated[12]. (6) The mantle flow field is used to advect the density field back in time from the present. (7) A geoid kernel (Fig. 1) is used to calculate the degree-two non-hydrostatic geoid from the density field at each time of the calculation. The opposite signs of the kernel in the upper and lower mantle mean that areas of low density in the lower mantle and of high density in the upper mantle cause positive geoid anomalies. (8) The difference between the actual and calculated degree-two geoid coefficients is added to obtain agreement of actual and calculated position of the pole at the present time. (9)

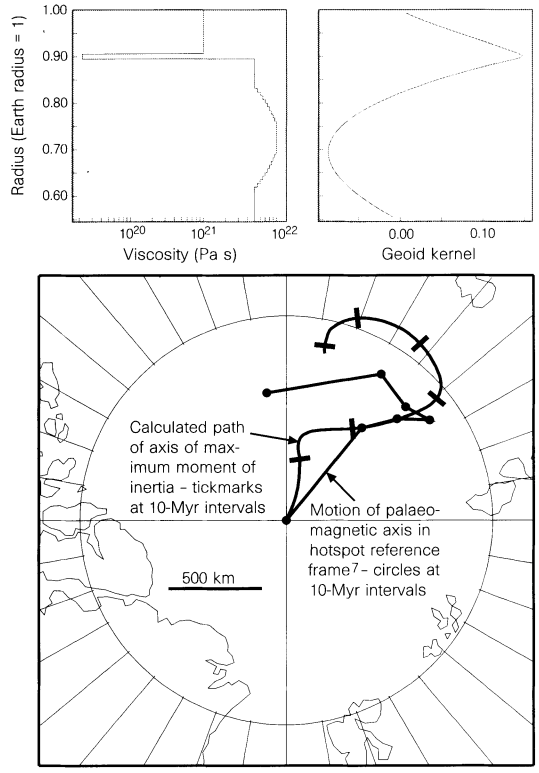

Figure 1 Change of the Earth's rotation axis: results of model calculation compared with palaeomagnetic results[7]. The model is based on flow in a viscous mantle driven by density heterogeneities inferred from the seismic tomography model SH12/WM13 (ref. 5); a conversion factor $(\delta\rho/\rho)/(\delta v/v) = 0.2$ from seismic velocity anomaly (v) to density anomaly (ρ) is used. This value is close to what has been proposed on theoretical grounds and from laboratory experiments[11], as well as from modelling the geoid[4]. The flow field is also constrained by realistic plate motions during the Cenozoic era; plate reconstructions[6] are inferred from sea-floor magnetic anomalies and hotspot traces. The viscosity model used (upper left) is based on models that reconcile the current geoid with tomographic models[4]. The geoid kernel (upper right), which includes the effects of compressibility[13], shows the relative contribution of density anomalies at a certain depth to the degree-two geoid[10,13] (which determines the moments of inertia). The calculated polar wander shown depends primarily on the bipolar nature of the geoid kernel as a function of depth. Any viscosity model that produced the same kernel function and had similar maximum viscosity would produce similar results. For other viscosity models considered, the calculated polar motion was too large to be consistent with observations, even if a very high viscosity ($\sim 10^{23}$ Pa s) in the lowermost mantle is assumed. For a larger conversion factor between seismic velocity and density, an increased magnitude of polar motion results, but the direction stays more or less the same. Other tomographic models give similar results, but SH12/WM13 produces the best overall fit. Flow in the upper mantle (largely related to plate motions) and flow in the lower mantle (mostly driven by internal density heterogeneities) produce contributions of similar magnitude to this process.

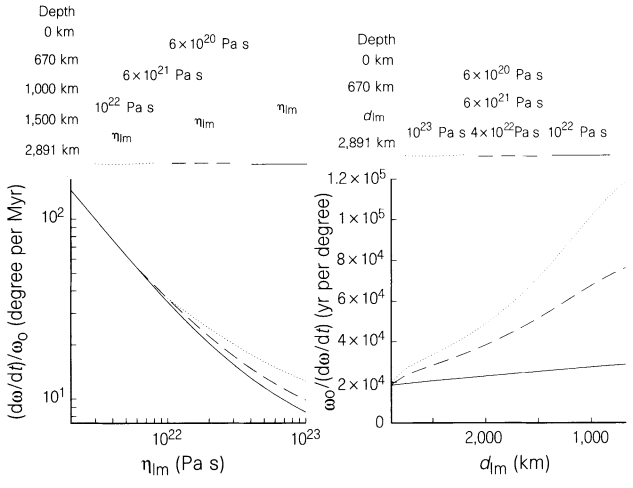

Figure 2 Rate of polar motion for a viscous, incompressible, rotating Earth model that was in hydrostatic equilibrium before a density heterogeneity corresponding to an inertia tensor element $J_{13} = 10^{33}$ kg m^2 was instantaneously imposed. The rate of polar motion $(d\omega/dt)/\omega_0$ plotted is the relatively uniform rate after initial transients have decayed, and is controlled by the rate at which the hydrostatic bulge can adjust to the changing rotation axis. The diurnal rotation rate is ω_0, and the model has a mantle of density 4,424 kg m^{-3} and a core of density 10,989 kg m^{-3}. Left-hand panel, the dependence on lower-mantle viscosity, η_{lm}; right-hand panel, the influence of the depth, at d_{lm}, at which viscosity increases in the lower mantle (this figure plots the inverse of the rate of polar motion). Similar results have been used previously to calculate rates of polar motion excited by random subducted slabs for a variety of Earth models[27].

The degree-two non-hydrostatic geoid is converted into the moment of inertia tensor by McCullagh's formula, and the principal axes are calculated.

These calculations are obviously approximate, but they are based on current dynamical models of mantle flow and dynamic support of the geoid[4,9,10,12,13]. The extension here has been to apply the model to previous times and plate configurations by advecting the density field backwards in time. This procedure should be accurate for relatively short times, although it will obviously break down for times longer than it would take a thermal anomaly to develop and rise or sink through most of the mantle. In a similar approach, subduction history has been used to calculate polar motion over an even longer time interval[14].

The rotation axis will follow the axis of the largest moment of inertia on a timescale governed by the readjustment of the rotational bulge. This in turn depends primarily on the viscosity structure of the mantle[3]. The following considerations most probably rule out a significant difference between rotation axis and axis of maximum moment of inertia.

The rotation axis tends to be nearly aligned with the axis of maximum total moment of inertia[2,3], which is the sum of the non-hydrostatic moment of inertia and the larger hydrostatic moment determined by the rotational bulge. The non-hydrostatic moment of inertia consists of an imposed part (which we calculated from the density and flow models) and a part that is due to the delayed viscoelastic relaxation of the bulge after a change of the rotation axis. As the axis of the imposed part of the inertia tensor moves, the rotation axis lags behind it by the angle[15]

$$\theta \approx \frac{\mathrm{d}\varphi}{\mathrm{d}t} \cdot \frac{1}{\Delta J_{\max} \cdot c_{\mathrm{tpw}}} \tag{1}$$

Here $\mathrm{d}\varphi/\mathrm{d}t$ is the rate at which the axis of the maximum imposed non-hydrostatic moment of inertia moves, $\Delta J_{\max}$ is the difference between maximum and minimum principal moments of inertia from the imposed mass anomalies, and the constant c_{tpw} describes the rate at which the bulge adjusts and hence the rate at which the true polar wander occurs in response to a change in the inertia tensor. It can be calculated for Earth models with various viscosity structures. If viscoelastic relaxation can be expressed in terms of eigenmodes, c_{tpw} can be expressed by

$$c_{\mathrm{tpw}}^{-1} = \sum_j \frac{c_{j0}}{s_j} J_j \tag{2}$$

where c_{j0} are the eigenmode expansion coefficients of the equilibrium shape minus the elastic deformation that would result if the Earth instantaneously started rotating at its present rate, s_j are decay constants and J_j are differences between maximum and minimum principal moments of inertia for these eigenmodes. Otherwise c_{tpw} may be determined numerically.

If a mass anomaly is emplaced suddenly, and the rotation vector is primarily in the z-direction, its rate of change will be given by

$$\frac{\mathrm{d}\omega_x}{\mathrm{d}t} = c_{\mathrm{tpw}} \omega_0 J_{13}^0 \tag{3}$$

where ω_0 is the diurnal rotation rate and J_{13}^0 is the non-diagonal inertia tensor component due to the emplaced non-hydrostatic excess masses. This equation applies to the quasi-steady state motion of the pole after initial transients have died out (that is, when the buildup of the non-hydrostatic shape due to the change in the rotation axis is exactly compensated for by viscoelastic decay of the old bulge).

Figure 2 shows the steady state rate of polar motion $(\mathrm{d}\omega_x/\mathrm{d}t)\cdot(1/\omega_0)$ caused by an imposed mass for a variety of Earth models. The rate (and hence c_{tpw}) is inversely proportional to the viscosity of the lower mantle, roughly inversely proportional to the thickness of a high-viscosity layer in the lower mantle and only slightly dependent on upper-mantle viscosity structure.

The Earth's rotation axis moved less than ~10° in the hotspot reference frame[7,16,17] during the past 50 Myr; equation (1) and inferred values of c_{tpw} from Fig. 2 show that the rotation pole would lag the inertia axis by $\theta < 1°$, even for models with $\eta \approx 10^{23}$ Pa s in the lower mantle.

It should be noted that equation (3) applies only if the emplacement of mass anomalies is rapid compared with the change of the rotation axis, as would be the case for a relatively high mantle viscosity. We can therefore estimate an upper bound to mantle viscosity. For the observed motion of ~10° in 50 Myr (refs 7, 16), the cases considered in Fig. 2, left, yield an upper bound to lower-mantle viscosity between about 3 and 5×10^{25} Pa s. This is not a stringent bound, as considerably slower motion of the rotation axis cannot be excluded[17], but it is similar to values obtained before[3].

If the mass anomalies are emplaced continuously at a rate corresponding to a growth rate of the inertia tensor component $\dot{J}_{13}$, the maximum rate of polar motion

$$\left.\frac{\mathrm{d}\omega}{\mathrm{d}t}\right|_{\max} \approx 0.47 \cdot \sqrt{\dot{J}_{13} c_{\mathrm{tpw}}} \tag{4}$$

occurs when the two larger principal non-hydrostatic moments of inertia are almost equal. The difference between instantaneous and gradual emplacement is illustrated in the bottom part of Fig. 3.

Figure 3 shows viscoelastic relaxation and corresponding changes in the rotation axis for a number of cases. We find that the speed at which the rotation axis moves is mainly determined by lower-mantle viscosity, whereas the effects of introducing an internal boundary or varying upper-mantle viscosity, and the effects of differences between viscous and viscoelastic Earth models, are all comparatively small.

The steady-state approximation is valid for times longer than the largest decay time. Unless internal modes are present (for example where there is a chemical boundary; Fig. 3) the largest decay time is small compared with timescales of polar wander, and steady-state is a good approximation. Furthermore, the magnitude of the effect of a chemical boundary is relatively small. We therefore conclude that for a realistic Earth model the angle θ is most likely to be small, even if polar motion is somewhat slowed by an internal chemical boundary[18,19], and the path of the axis of maximum imposed moment of inertia can be compared directly with palaeomagnetic results[7].

Observations of polar wander have been inferred from palaeomagnetic apparent polar wander paths, assuming that the rotation and palaeomagnetic axes are essentially the same[20]. If there were no plate motions, the interpretation of these would be straightforward, but the determination of polar wander on a planet with a mobile surface is more complicated. Two reference frames have been proposed for plate motions: a mean lithospheric frame, which is the average of all plate motions, and a hotspot frame that assumes that hotspots are fixed in location by a lower mantle that is essentially stationary relative to plate motions. Early work suggested that there is no significant motion of the rotation axis in the mean lithospheric frame[21,22], whereas there is motion of the rotation axis with respect to the hotspot frame[23]. More recent results, however, indicate that both reference frames and the rotation axis all move with respect to each other[24]. Results from models of plumes and hotspots indicate similar motions[15].

The comparison between the model results and palaeomagnetic observations of polar wander is shown in Fig. 1. The scatter between the palaeomagnetic curves from individual continents is larger than the average motion[16], and there are also substantial differences between results by various authors[7,16,17]. The good agreement between modelled and observed polar motion in Fig. 1 was obtained with a geoid kernel that reverses sign, with roughly equal magnitude on either side, as shown in Fig. 1; this behaviour is a consequence of the viscosity model used, which has also been used to model the present geoid[4].

The rate of polar motion in recent times has been directly

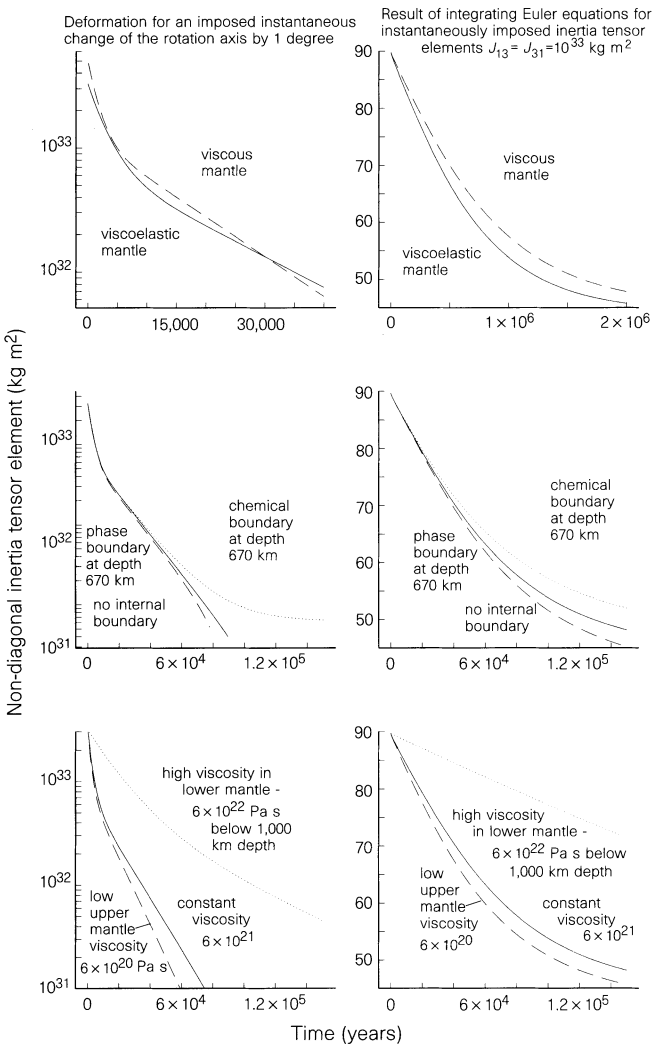

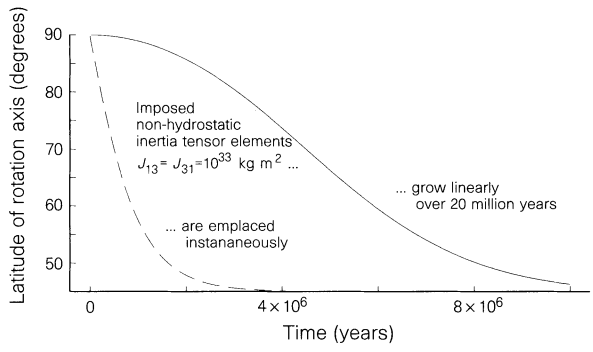

Figure 3 The effects of various model parameters on viscoelastic relaxation and the motion of the rotation axis. Left, the non-diagonal inertia tensor components as a function of time following a 1° shift of the rotation axis. Right, the motion of the rotation pole following the emplacement of density heterogeneities that ultimately drive the pole to move 45°. Top row, a viscous incompressible mantle (as in Fig. 2) is compared with a viscoelastic mantle parameterized as a PREM (ref. 28) lower mantle. Viscosity is 10^{21} Pa s. Because of the instantaneous elastic deformation, there is an offset of the two curves at time zero in the left plot, and the rotation axis moves faster in the viscoelastic case. Second row, the effects of an internal boundary at 670 km depth. The density parameters above the boundary are as in PREM between 5,701 and 5,771 km. Shown are the effects of an equilibrium phase boundary and a chemical boundary with a density contrast. This latter models shown a very slow relaxation mode. The calculated polar motion is initially similar in all cases, but the curve for a chemical boundary layer flattens out faster, as steady state is approached, corresponding to previous results that find polar motion to be significantly slower for a chemical than for a phase boundary[18,19]. Third row, the effects of various viscosity models; all other parameters similar to the viscoelastic case in the top row. Fourth row, the time response for instantaneous emplacement of density heterogeneity compared with the response when the heterogeneity grows linearly over 20 Myr. These results were obtained using a time domain approach[15,29] for a mantle with a Maxwell viscoelastic rheology.

measured by astronomical and geodetic techniques[8], and it is roughly in accord with the longer-term motion inferred from palaeomagnetic observations[25]. The current polar motion is an important constraint on current models of mantle rheology inferred from observations of post-glacial isostatic readjustment[26,30]. Our results yield a current rate of polar motion of 0.39° per Myr towards 24W, with an average of 0.37° per Myr towards 24W over the past 1 Myr. This is a substantial fraction of the value 0.95° per Myr towards 76W that is used to constrain rebound models[26]. Figure 1 shows that rates of this magnitude characterize the polar motion inferred from palaeomagnetic results as well as the model results for the past 50 Myr or so. Thus a considerable fraction of the current polar motion may represent a secular trend that has existed for millions of years. The effects of post-glacial rebound would be superposed on the long-term trend. Coincidentally, the two motions are similar[25]. Clearly both effects need to be well understood to interpret the current observations properly.

It is apparent that a plausible model of mantle viscosity, coupled with the time-dependent density distribution implied by the model, can account for long-term polar wander similar to that observed. Similar models can predict polar motion that is considerably faster than observed as well. The remarkable thing about true polar wander may not be that it occurs, but that it is so slow. Our current models of the Earth's mantle, however, allow us to predict the polar wander path reasonably well. □

Received 31 October 1996; accepted 18 March 1997.

1. Gold, T. Instability of the Earth's axis of rotation. *Nature* **175,** 526–529 (1955).
2. Munk, W. & MacDonald, G. J. F. *The Rotation of the Earth* (Cambridge Univ. Press, New York, 1960).
3. Goldreich, P. & Toomre, A. Some remarks on polar wandering. *J. Geophys. Res.* **74,** 2555–2567 (1969).
4. Forte, A. M., Dziewonski, A. M. & Woodward, R. L. *Aspherical structure of the mantle, tectonic plate motions, nonhydrostatic geoid and topography of the core–mantle boundary* in *Dynamics of the Earth's Deep Interior and Earth Rotation, Geophys. Mon. Ser.* Vol. 72, (eds Le Mouël, J.-L. *et al.*) 135–166 (AGU, Washington DC, 1994).
5. Su, W., Woodward, R. L. & Dziewonski, A. M. Degree 12 model of shear velocity heterogeniety in the mantle. *J. Geophys. Res.* **99,** 6945–6980 (1994).
6. Gordon, R. G. & Jurdy, D. M. Cenozoic global plate motions. *J. Geophys. Res.* **91,** 12389–12406 (1986).
7. Besse, G. & Courtillot, V. Revised and synthetic apparent polar wander paths of the African, Eurasian, North American and Indian plates, and true polar wander since 200 Ma. *J. Geophys. Res.* **96,** 4029–4050 (1991).
8. Dickman, S. R. Secular trends in the Earth's rotation pole: Consideration of the motion of latitude observatories. *Geophys. J. R. Astron. Soc.* **51,** 229–224 (1977).
9. Hager, B. H., Clayton, R. W., Richards, M. A., Comer, R. P. & Dziewonski, A. M. Lower mantle heterogeneity, dynamic topography and the geoid. *Nature* **313,** 541–545 (1985).
10. Richards, M. & Hager, B. Geoid anomalies in a dynamic Earth. *J. Geophys. Res.* **89,** 5987–6002 (1984).
11. Karato, S. Importance of anelasticity in the interpretation of seismic tomography. *Geophys. Res. Lett.* **20,** 1623–1626 (1993).
12. Hager, B. H. & O'Connell, R. J. A simple global model of plate dynamics and mantle convection. *J. Geophys. Res.* **86,** 4843–4867 (1981).
13. Panasyuk, S. V., Hager, B. H. & Forte, A. M. Understanding the effects of mantle compressibiity on geoid kernels. *Geophys. J. Int.* **124,** 121–133 (1996).
14. Richards, M. A., Ricard, Y., Lithgow-Bertelloni, C., Spada, G. & Sabadini, R. An explanation for Earth's long-term rotational stability. *Science* **275,** 372–375 (1997).
15. Steinberger, B. M. Motion of hotspots and changes of the Earth's rotation axis caused by a convecting mantle. Thesis, Univ. Harvard (1996).
16. Andrews, J. A. True polar wander: An analysis of cenozoic and mesozoic paleomagnetic poles. *J. Geophys. Res.* **90,** 7737–7750 (1985).
17. Livermore, R. A., Vine, F. J. & Smith, A. G. Plate motions and the geomagnetic field, II, Jurassic to Tertiary. *Geophys. J. R. Astron. Soc.* **79,** 939–961 (1984).
18. Ricard, Y. & Sabadini, R. Rotational instabilities of the Earth induced by mantle density anomalies. *Geophys. Res. Lett.* **17,** 627–630 (1990).
19. Sabadini, R. & Yuen, D. A. Mantle stratification and long-term polar wander. *Nature* **339,** 373–375 (1989).
20. Tarling, D. H. *Principles and Applications of Paleomagnetism* (Chapman and Hall, London, 1971).
21. McElhinny, M. W. Mantle plumes, palaeomagnetism and polar wandering. *Nature* **241,** 523–528 (1973).

22. Jurdy, D. M. & Van der Voo, R. A method for the separation of true polar wander and continental drift including results for the last 55 m.y. *J. Geophys. Res.* **79,** 2945–2952 (1974).
23. Duncan, R. A., Petersen, N. & Hargraves, R. B. Mantle plumes, movement of the European plate and polar wandering. *Nature* **239,** 82–86 (1972).
24. Gordon, R. G. & Livermore, R. A. apparent polar wander of the mean-lithosphere reference frame. *Geophys. J. R. Astron. Soc.* **91,** 1049–1057 (1987).
25. Gordon, R. G. Plate motions, crustal and lithospheric mobility, and paleomagnetism: Prospective viewpoint. *J. Geophys. Res.* **100,** 24367–24392 (1995).
26. Peltier, W. R. & Jiang, X. Glacial isostatic adjustment and Earth rotation: Refined constraints on the viscosity of the deepest mantle. *J. Geophys. Res.* **101,** 3269–3290 (1996).
27. Spada, G., Ricard, Y. & Sabadini, R. Excitation of true polar wander by subduction. *Nature* **360,** 452–454 (1992).
28. Dziewonski, A. M. & Anderson, D. L. Preliminary Reference Earth Model. *Phys. Earth Planet. Inter.* **25,** 297–356 (1981).
29. Hanyk, L., Moser, J., Yuen, D. A. & Matyska, C. Time-domain approach for the transient responses in stratified viscoelastic Earth. *Geophys. Res. Lett.* **22,** 1285–1288 (1995).
30. Mitrovica, J. X. & Forte, A. M. Radial profile of mantle viscosity: Results from the joint inversion of convection and post-glacial rebound observables. *J. Geophys. Res.* **102,** 2751–2769 (1997).

Acknowledgements. We thank S. V. Panasyuk for calculating the geoid kernels for us, and J. X. Mitrovica for a review. This work was supported by the NSF.

Correspondence should be addressed to B.S. (e-mail: steinber@geophysik.uni-frankfurt.de).

Body mass and encephalization in Pleistocene *Homo*

Christopher B. Ruff*, Erik Trinkaus† & Trenton W. Holliday‡

** Department of Cell Biology and Anatomy, Johns Hopkins University School of Medicine, 725 North Wolfe Street, Baltimore, Maryland 21205, USA*
† Department of Anthropology, University of New Mexico, Albuquerque, New Mexico 87131, USA, and URA 376 du C.N.R.S., Université de Bordeaux I, 33405 Talence, France
‡ Department of Anthropology, College of William and Mary, Williamsburg, Virginia 23187-8795, USA

Many dramatic changes in morphology within the genus *Homo* have occurred over the past 2 million years or more, including large increases in absolute brain size and decreases in postcanine dental size and skeletal robusticity. Body mass, as the 'size' variable against which other morphological features are usually judged, has been important for assessing these changes[1–5]. Yet past body mass estimates for Pleistocene *Homo* have varied greatly, sometimes by as much as 50% for the same individuals[2,3,6–12]. Here we show that two independent methods of body-mass estimation yield concordant results when applied to Pleistocene *Homo* specimens. On the basis of an analysis of 163 individuals, body mass in Pleistocene *Homo* averaged significantly (about 10%) larger than a representative sample of living humans. Relative to body mass, brain mass in late archaic *H. sapiens* (Neanderthals) was slightly smaller than in early 'anatomically modern' humans, but the major increase in encephalization within *Homo* occurred earlier during the Middle Pleistocene (600–150 thousand years before present (kyr BP)), preceded by a long period of stasis extending through the Early Pleistocene (1,800 kyr BP).

It is generally acknowledged, even by those who have used other methods, that the best means of estimating body mass from skeletal or fossil remains, when feasible, is to use features that have some direct functional relationship to body mass[9,11,12]. For hominids, the skeletal dimensions used most often have been lower limb long bone diaphyseal and articular breadths[2,3,6,7,9]. Diaphyseal breadths of fossil hominids are problematic as body mass estimators because relative to body size they are systematically larger than modern humans, probably as a response to increased mechanical loading[5]. In contrast, articulations are much less environmentally sensitive[13,14], and thus are potentially better body-size indicators. The articular dimension used here as a body-mass estimator is femoral head breadth because it is available for many fossil *Homo* specimens, is easily measured and highly reproducible, and because several investigators have provided information on the relationship between femoral head breadth and body mass in modern humans[6,13,15] (see Methods).

The second method used here to estimate body mass does not rely on any assumptions about the mechanical relationship between a particular skeletal feature and body size (support of body weight). Rather, in this approach body mass is estimated directly from reconstructed stature and body breadth. A modern worldwide anthropometric sampling of 56 population/sex-specific means[16] was used to derive multiple regressions of body mass on stature and bi-iliac (maximum pelvic) breadth (Methods).

Figure 1 compares femoral head and stature/bi-iliac estimates of body mass for 75 Pleistocene *Homo* specimens. The mean absolute difference between estimates is about 5 kg (7.6%), and the mean directional difference is less than 1 kg (1.1%). Paired *t*-tests between results are not significant ($P \geq 0.30$). Thus, equations based on femoral head size and stature/bi-iliac breadth yield similar body mass estimates when applied to Pleistocene *Homo*, with very little systematic bias. Because the two techniques are based on different rationales and skeletal dimensions, yet nevertheless converge on the same result, this increases confidence in both.

Skeletal dimensions for 163 Pleistocene *Homo* specimens, dated 10–1,950 kyr BP, were derived from previously published sources and personal measurements[5,10,17]. Most regions of the Old World (except Australia) are represented, although the majority of the sample is from Europe (55%), with the remainder from Africa (27%), western Asia (15%) and eastern Asia (3%). (Data for individual specimens are given in Supplementary Information.) The resulting body mass estimates are shown in Fig. 2a, together with 51 sex/population-specific means for a worldwide sampling of living humans (ref. 16, excluding five Pygmy data points). More than three-quarters (125/163) of the Pleistocene specimens fall above the living human mean. On average, Pleistocene specimens are 7.4 kg larger (mean ± s.e., 65.6 ± 0.7 kg) than living humans (58.2 ± 1.0 kg), a highly significant 12.7% difference in body mass ($P < 0.0001$, *t*-test).

There is some indication in Fig. 2a that body mass is lower in the Early Pleistocene and rises to peak values in the Late Pleistocene. However, this is largely an artefact of two confounding variables: sex

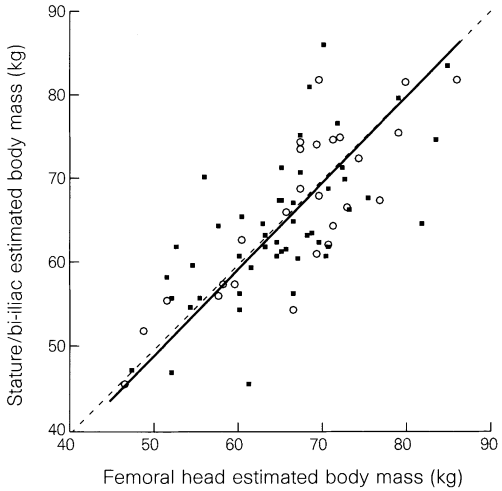

Figure 1 Comparison between body mass estimated from stature and bi-iliac breadth, and body mass estimated from femoral head breadth in 75 Pleistocene *Homo* specimens. Empty symbols, measured bi-iliac breadth; filled symbols, estimated bi-iliac breadth. Solid line, reduced major axis regression ($y = 1.04 \times x - 3.4$; $r = 0.738$). Dotted line indicates equivalence of y and x.